Biomedical Optics EXPRESS

Identification of vessel wall degradation in ascending thoracic aortic aneurysms with OCT

Eusebio Real,[1,*] José Fernando Val-Bernal,[2] José M. Revuelta,[3] Alejandro Pontón,[4] Marta Calvo Díez,[4] Marta Mayorga,[2] José M. López-Higuera,[1] and Olga M. Conde[1]

[1] Department TEISA, Photonics Engineering Group University of Cantabria, Avda. Los Castros S/N, 39005 Santander, Spain

[2]IDIVAL and Anatomical Pathology Department, Marqués de Valdecilla University Hospital, Medical Faculty, University of Cantabria, Avda.Valdecilla S/N 39008, Santander, Spain

[3]Medical and Surgical Sciences Department. Faculty of Medicine. University of Cantabria, Avda.Cardenal Herrera Oria S/N 39011, Santander, Spain

[4]Cardiovascular Surgery Service. Marqués de Valdecilla University Hospital, Avda.Valdecilla S/N 39008, Santander, Spain

[*]eusebio.real@unican.es

Abstract: Degradation of the wall of human ascending thoracic aorta has been assessed through Optical Coherence Tomography (OCT). OCT images of the media layer of the aortic wall exhibit micro-structure degradation in case of diseased aortas from aneurysmal vessels. The OCT indicator of degradation depends on the dimension of areas of the media layer where backscattered reflectivity becomes smaller due to a disorder on the morphology of elastin, collagen and smooth muscle cells (SMCs). Efficient pre-processing of the OCT images is required to accurately extract the dimension of degraded areas after an optimized thresholding procedure. OCT results have been validated against conventional histological analysis. The OCT qualitative assessment has achieved a pair sensitivity-specificity of 100%-91.6% in low-high degradation discrimination when a threshold of 4965.88μm^2 is selected. This threshold suggests to have physiological meaning. The OCT quantitative evaluation of degradation achieves a correlation of 0.736 between the OCT indicator and the histological score. This in-vitro study can be transferred to the clinical scenario to provide an intraoperative assessment tool to guide cardiovascular surgeons in open repair interventions.

OCIS codes: (170.4500) Optical coherence tomography; (170.6935) Tissue characterization.

References and links

1. Y. Masuda, Z. Yamada, N. Morooka, S. Watanabe, and Y. Inagaki, "Prognosis of patients with medically treated aortic dissections," Circulation **84**(5 Suppl), III7–III13 (1991).
2. L. de Figueiredo Borges, R. G. Jaldin, R. R. Dias, N. A. G. Stolf, J. B. Michel, and P. S. Gutierrez, "Collagen is reduced and disrupted in human aneurysms and dissections of ascending aorta," Hum. Pathol. **39**(3), 437–443 (2008).
3. R. G. Koch, A. Tsamis, A. D'Amore, W. R. Wagner, S. C. Watkins, T. G. Gleason, and D. A. Vorp, "A custom image-based analysis tool for quantifying elastin and collagen micro-architecture in the wall of the human aorta from multi-photon microscopy," J. Biomech. **47**(5), 935–943 (2014).
4. A. Tsamis, J. A. Phillippi, R. G. Koch, S. Pasta, A. D'Amore, S. C. Watkins, W. R. Wagner, T. G. Gleason, and D. A. Vorp, "Fiber micro-architecture in the longitudinal-radial and circumferential-radial planes of ascending thoracic aortic aneurysm media," J. Biomech. **46**(16), 2787–2794 (2013).
5. S. Pasta, J. A. Phillippi, T. G. Gleason, and D. A. Vorp, "Effect of aneurysm on the mechanical dissection properties of the human ascending thoracic aorta," J. Thorac. Cardiovasc. Surg. **143**(2), 460–467 (2012).
6. L. F. Hiratzka, G. L. Bakris, J. A. Beckman, R. M. Bersin, V. F. Carr, D. E. Casey, K. A. Eagle, L. K. Hermann, E. M. Isselbacher, E. A. Kazerooni, N. T. Kouchoukos, B. W. Lytle, D. M. Milewicz, D. L. Reich, S. Sen, J. A. Shinn, L. G. Svensson, and D. M. Williams, "Guidelines for the diagnosis and management of patients with thoracic aortic disease: executive summary," J. Am. Coll. Cardiol. **55**, 1509–1544 (2010).
7. R. Cicchi, C. Matthäus, T. Meyer, A. Lattermann, B. Dietzek, B. R. Brehm, J. Popp, and F. S. Pavone, "Characterization of collagen and cholesterol deposition in atherosclerotic arterial tissue using non-linear microscopy," J. Biophotonics **7**(1-2), 135–143 (2014).

#220039 - $15.00 USD Received 1 Aug 2014; revised 10 Oct 2014; accepted 14 Oct 2014; published 29 Oct 2014

8. M. E. Brezinski, G. J. Tearney, B. E. Bouma, J. A. Izatt, M. R. Hee, E. A. Swanson, J. F. Southern, and J. G. Fujimoto, "Optical coherence tomography for optical biopsy. Properties and demonstration of vascular pathology," Circulation **93**(6), 1206–1213 (1996).
9. H. Yabushita, B. E. Bouma, S. L. Houser, H. T. Aretz, I. K. Jang, K. H. Schlendorf, C. R. Kauffman, M. Shishkov, D. H. Kang, E. F. Halpern, and G. J. Tearney, "Characterization of human atherosclerosis by optical coherence tomography," Circulation **106**(13), 1640–1645 (2002).
10. S. Tahara, T. Morooka, Z. Wang, H. G. Bezerra, A. M. Rollins, D. I. Simon, and M. A. Costa, "Intravascular optical coherence tomography detection of atherosclerosis and inflammation in murine aorta," Arterioscler. Thromb. Vasc. Biol. **32**(5), 1150–1157 (2012).
11. J. M. Schmitt, A. Knüttel, M. Yadlowsky, and M. A. Eckhaus, "Optical-coherence tomography of a dense tissue: statistics of attenuation and backscattering," Phys. Med. Biol. **39**(10), 1705–1720 (1994).
12. J. G. Fujimoto, S. A. Boppart, G. J. Tearney, B. E. Bouma, C. Pitris, and M. E. Brezinski, "High resolution in vivo intra-arterial imaging with optical coherence tomography," Heart **82**(2), 128–133 (1999).
13. N. A. Patel, X. Li, D. L. Stamper, J. G. Fujimoto, and M. E. Brezinski, "Guidance of aortic ablation using optical coherence tomography," Int. J. Cardiovasc. Imaging **19**(2), 171–178 (2003).
14. K. C. Hoang, A. Edris, J. Su, D. S. Mukai, S. Mahon, A. D. Petrov, M. Kern, C. Ashan, Z. Chen, B. J. Tromberg, J. Narula, and M. Brenner, "Use of an oxygen-carrying blood substitute to improve intravascular optical coherence tomography imaging," J. Biomed. Opt. **14**(3), 034028 (2009).
15. D. P. Popescu, C. Flueraru, Y. Mao, S. Chang, and M. G. Sowa, "Signal attenuation and box-counting fractal analysis of optical coherence tomography images of arterial tissue," Biomed. Opt. Express **1**(1), 268–277 (2010).
16. E. Real, A. Eguizábal, A. Pontón, M. C. Díez, J. Fernando Val-Bernal, M. Mayorga, J. M. Revuelta, J. M. López-Higuera, and O. M. Conde, "Optical coherence tomography assessment of vessel wall degradation in thoracic aortic aneurysms," J. Biomed. Opt. **18**(12), 126003 (2013).
17. H. S. Cho, S. J. Jang, K. Kim, A. V. Dan-Chin-Yu, M. Shishkov, B. E. Bouma, and W. Y. Oh, "High frame-rate intravascular optical frequency-domain imaging in vivo," Biomed. Opt. Express **5**(1), 223–232 (2014).
18. F. J. van der Meer, D. J. Faber, I. Çilesiz, M. J. C. van Gemert, and T. G. van Leeuwen, "Temperature-dependent optical properties of individual vascular wall components measured by optical coherence tomography," J. Biomed. Opt. **11**(4), 041120 (2006).
19. C. L. Berry, J. A. Sosa-Melgarejo, and S. E. Greenwald, "The relationship between wall tension, lamellar thickness, and intercellular junctions in the fetal and adult aorta: its relevance to the pathology of dissecting aneurysm," J. Pathol. **169**(1), 15–20 (1993).
20. J. F. Matthias Bechtel, F. Noack, F. Sayk, A. W. Erasmi, C. Bartels, and H. H. Sievers, "Histopathological grading of ascending aortic aneurysm: comparison of patients with bicuspid versus tricuspid aortic valve," J. Heart Valve Dis. **12**(1), 54–59 (2003).
21. N. Otsu, "A Threshold Selection Method from Gray-Level Histograms," IEEE Sys Man Cyb **9**(1), 62–66 (1979).
22. P. Kovesi, "Phase Preserving Denoising of Images," The Australian Pattern Recognition Society Conference: DICTA'99 212–217 (1999).
23. P. Kovesi, MATLAB and Octave Functions for Computer Vision and Image Processing," Csse,May 2000, <http://www.csse.uwa.edu.au/~pk/research/matlabfns/>, (12 November 2013).
24. I. Fine, E. Loewinger, A. Weinreb, and D. Weinberger, "Optical properties of the sclera," Phys. Med. Biol. **30**(6), 565–571 (1985).
25. R. Drezek, A. Dunn, and R. Richards-Kortum, "Light scattering from cells: finite-difference time-domain simulations and goniometric measurements," Appl. Opt. **38**(16), 3651–3661 (1999).
26. E. A. Genina, A. N. Bashkatov, and V. V. Tuchin, "Tissue optical immersion clearing," Expert Rev. Med. Devices **7**(6), 825–842 (2010).

1. Introduction

Soft fibrous tissues such as the aortic wall rely on a complex fiber micro-architecture to provide a high degree of elasticity or compliance. The alteration of its constituents, collagen and elastin, impair the functional behavior of these tissues inducing ascending aortic diseases such as aneurysms or dissections highly mortal due to the rupture of the vessel [1]. Aortic dissections and ascending aorta aneurysms share the same histopathologic features, situated at the medial layer namely, increase in mucoid substance, fragmentation of elastic fibers, and apparent reduction in the number of smooth muscle cells [2]. A possible mechanism for dissection [3] is that blood pressure-induced stresses exceed the adhesive strength that holds the elastic layers together [4]. The resistance to delamination may be affected by the interlaminar elastin and collagen fibers which are radially-orientated. Therefore, in the degenerated wall, the forces developed by hemodynamics may exceed the adhesive forces holding the mural layers together, likely inducing spontaneous tears in the intimal-medial interface or in the medial layer of the weakened aorta [5].

From a clinical point of view, thoracic aortic aneurysm diagnosis relies on aorta diameter measurement through imaging techniques such as X-rays and echography [6]. During open aneurysm repair [6], where blood is not present, cardiovascular surgeons must select the area

#220039 - $15.00 USD Received 1 Aug 2014; revised 10 Oct 2014; accepted 14 Oct 2014; published 29 Oct 2014

of the resected tissue. Decisions about an extension to aortic arch surgery may depend on the actual degradation of the vessel wall. In asymptomatic patients with ascending aortic aneurysm, this degradation is not always manifested through the diameter enlargement [6] so an alternative assessment technique is advisable. The conventional histopathological analysis provides the gold standard to evaluate the quality of the aortic wall [2], but its implementation is not straightforward during intervention. Optical techniques such as multiphoton microscopy [3, 4] have assessed the degradation of the aortic wall with penetrations of 200μm and, when combined with coherent anti-Stokes Raman spectroscopy is able to distinguish collagen from cholesterol in atherosclerotic arterial tissue [7] quantifying the fiber size, distribution and anisotropy of collagen in healthy arterial wall and in atherosclerotic plaque using image pattern evaluation algorithms. Optical Coherence Tomography, able to provide depth penetrations of 2 mm, has been also applied to arterial wall analysis but mainly focused in the assessment of different types of atherosclerotic plaques in coronary arteries (fibrous, fibrocalcific, lipid rich) [8–10] more than in aortic arteries. Few studies have been found dealing with the OCT characterization of the aortic wall [11–15] most of them related to animal samples and little to human aortas [13].

In a previous work [16], an in-vitro study for the identification of aneurysmal aortic walls in human samples was presented. The textural analysis of OCT image sections of the media layer of the aortic wall revealed the anomalies present in the wall micro-structure. In [16] an identification rate with a sensitivity-specificity of 90%-86% was reached. Now, the aim of the present study is to improve this identification outcome and to gain insight of the degradation of the aortic wall validating the OCT analysis with the physiological analysis provided by conventional histopathology. The goal is to develop a custom, image-based analysis tool able to identify and to quantify the level of degradation of aortic walls using OCT images. The final application of the tool would be to help guide intraoperative surgery to properly locate and resect the entered diseased aortic wall and graft replacement, so preventing further postoperative complications and consequently to improve patient prognosis. The present tool can be employed in the clinics because, in open surgery interventions, no blood circulation is present in the intraoperative cavity. This in-vitro proof-of-principle could be transferred to in-vivo assessment provided a fast OCT system and the appropriate catheter [17]. Moreover, the conclusions regarding the wall degradation assessment though OCT evaluation could be also transferred to other clinical scenarios: carotid arteries, aorto-iliac or ilio-femoral sections, etc. where blood can be flushed or temporally eliminated more efficiently than into the aorta.

2. Materials and methods

2.1 Optical coherence tomography

Human aortic samples were interrogated with the bench-top OCT system Thorlabs OCS1300SS. The light source is a swept source with center wavelength of 1325 nm and 100nm bandwidth at half maximum. Provided sensitivity is up to 100dB. The resolution of the system is of 12μm in depth and 25μm lateral, for a maximum B-scan dimension of 3 mm and 10mm respectively. Resulting images are sampled with 512 pixels in depth by 1024 pixels lateral. The axial resolution corresponds to air penetration conditions for 3mm penetration. In this case, the media layer refraction index is of 1.38 [18] giving a final pixel resolution of 4.24μm/pixel axial. Lateral pixel resolution results 9.76 μm/pixel.

Aorta specimens were conserved in phosphate buffered saline (PBS) before the OCT analysis and were hydrated during the measurement procedure. The samples of each patient are divided in different regions of analysis (ROI) to provide a characterization throughout the whole sample. These ROIs are taken along and across the blood flow through the vessel lumen. Every ROI is measured with the OCT system, obtaining a C-scan or 3D cube (10x10mm). This cube consists of several cross-sectional images, called B-scan (3x10mm, 512x1024pixels), which are the target for the purposed study. Five B-scans are obtained for each ROI, at the positions central, +/–2mm and +/–5mm (Fig. 1). The B-scan is the reference data and consists of gray level images taking values from 0 to 255 (8-bits). The system

#220039 - $15.00 USD Received 1 Aug 2014; revised 10 Oct 2014; accepted 14 Oct 2014; published 29 Oct 2014

response has been characterized. The obtained Point Spread Function (PSF) and sensitivity decay within depth have been taken into account and a correction is applied for every acquired image [16]. The probe lens focal point is placed on the surface of the sample in order characterize the media layer from the surface. According to theoretical calculations [19], the capacity to sustain stress is greater at the internal two thirds of the media (900 μm), leaving an abrupt interface at the external third (from 900 μm to 1350 μm). The capacity of OCT to penetrate into tissue allows visualizing this part of the aortic wall where an impairment of the micro-structure can result in mortality.

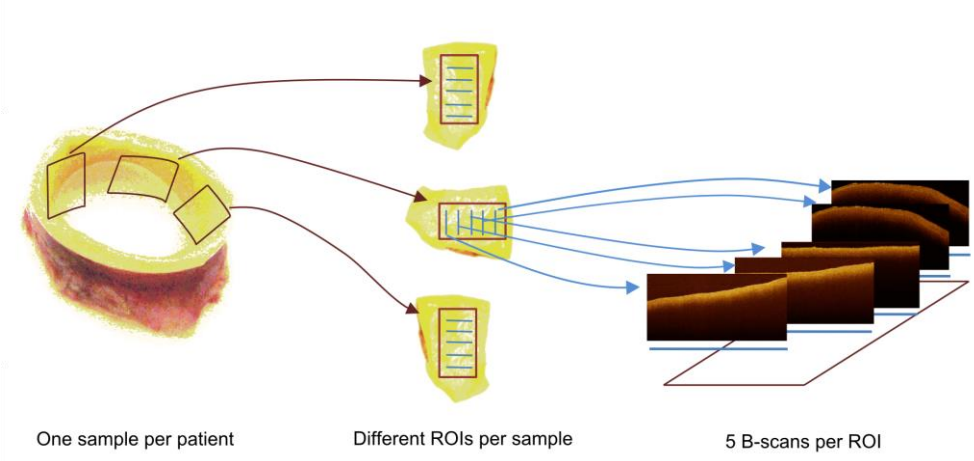

Fig. 1. Sample processing schematic. Every sample is divided into several Regions Of Interest (ROI). On every ROI, 5 OCT B-scans were obtained.

2.2 Histopathology

This study is focused on the ascending thoracic aorta section, as different regions of the aorta artery may have different structure and composition, besides wall degradation. The aorta sample set consists of 28 specimens from different patients, belonging to two groups: heart transplantation donors (10 samples) and aneurysm surgical interventions patients (18 samples). Heart donors were selected according to standard cardiac donation criteria, being younger than 55 years and not presenting previous heart or vascular diseases. Aneurysm patients went through thoracic aneurysm surgical repair intervention (Bentall or Wheat procedures [6]), according to cardiovascular surgeons criteria.

After OCT analysis of the samples, an expert pathologist employs common histological staining techniques. Hematoxylin and Eosin (H&E) method was performed to reveal all tissue structures, Masson's trichrome stain was used for collagen, Verhoeff's Van Gieson (EVG) for elastic fibers, Alcian Blue (AB) at pH 2.5 to remark acidic polysaccharides and mucopolysaccharides, and Alpha-Smooth Muscle Actin (α-SMA) to visualize the SMCs structure. The staining process is time consuming and complicated assuming the dimensions of the aorta wall. For that reason, only one portion of the sample is measured with these techniques. This analysis is applied to the closest regions where the OCT images were measured, so as to be able to correlate results from both analyses. For that aim, the area measured with the OCT setup was delimited with India ink.

Samples belonging to both groups exhibit different wall degradation severity: not every pathological sample shows severe degradation and, on the other hand, not every donor sample is completely healthy. For that reason, a semi-quantitative grading scheme for the histopathological grading has been applied [20]. This grading scheme quantifies degradation accounting for elastic fiber fragmentation, fibrosis, medio-necrosis, cystic change and SMCs structure. Each of these classes is evaluated independently, grading degradation from 0 (no degradation) to 3 (severe degradation), according to the fault dimension in relation to the wall

#220039 - $15.00 USD Received 1 Aug 2014; revised 10 Oct 2014; accepted 14 Oct 2014; published 29 Oct 2014

thickness and the size of a lamellar unit. The mean values of these parameters measured during the histological analysis of the current samples set are of 1349.69 µm (σ = 277.35µm) for the media thickness and 16.8µm (σ = 4.75µm) for the lamellar unit dimension. The addition of the five classes provides a total score from 0 to 15. According to the samples in the data set and, as a consensus with the pathologists and surgeons, this score is used to divide the sample set into two new categories (Table 1): category 1 (scores 0 to 7) showing low degradation and category 2 (scores 8 to 15) showing severe degradation (Fig. 2). Table 1 shows the mean degradation for each marker and category.

Table 1. Histological quantification of individual disorders, computed 0 to 3, and resulting histological score. Mean values per category are shown for comparison.

	Degradation					
	Fibrosis	**Necrosis**	**Cystic change**	**Elastic fragmentation**	**SMC orientation**	**Total score**
Category 1	0.45/3	0.83/3	1.16/3	0.25/3	0.00/3	**2.66/15**
Category 2	1.50/3	1.50/3	3.00/3	2.75/3	2.00/3	**10.75/15**

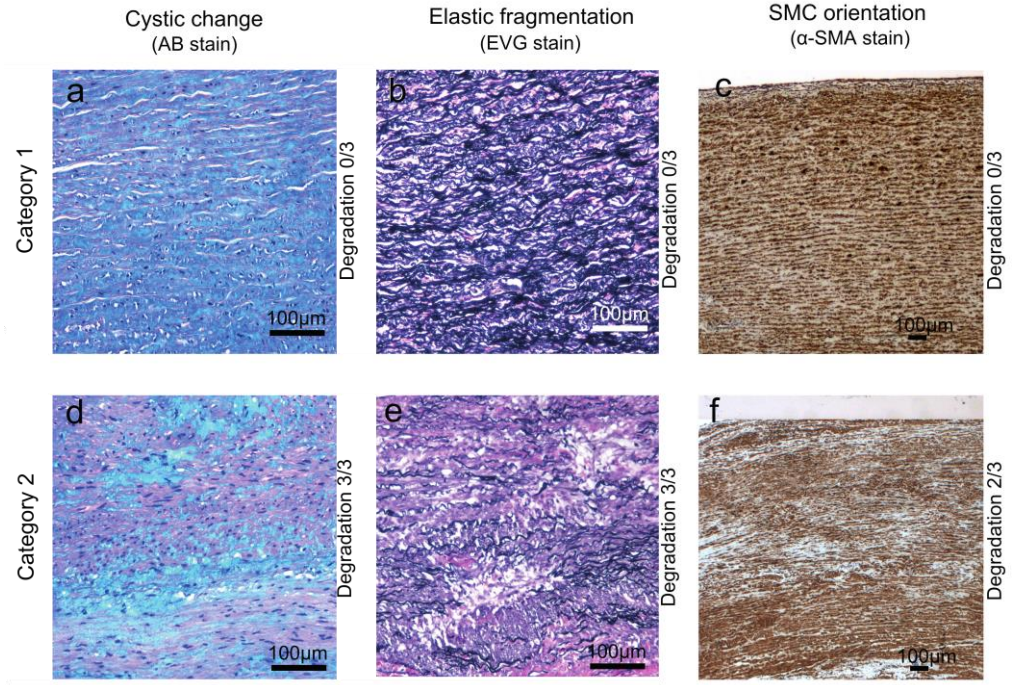

Fig. 2. Histological images for score grading. Different staining techniques are applied to visualize different degradation effects. Category 1 (a,b,c) and 2 (d,e,f) are shown for comparison.

2.3 B-scan processing

The proposed method is aimed to identify reflectivity anomalies in the measured B-scans. In order to automatize the process, every image is pre-processed for the anomaly detection algorithm optimization. The preprocessing method consists of automatic image correction, segmentation of the region of interest and thresholding to delimit anomalies (Fig. 3).

#220039 - $15.00 USD Received 1 Aug 2014; revised 10 Oct 2014; accepted 14 Oct 2014; published 29 Oct 2014

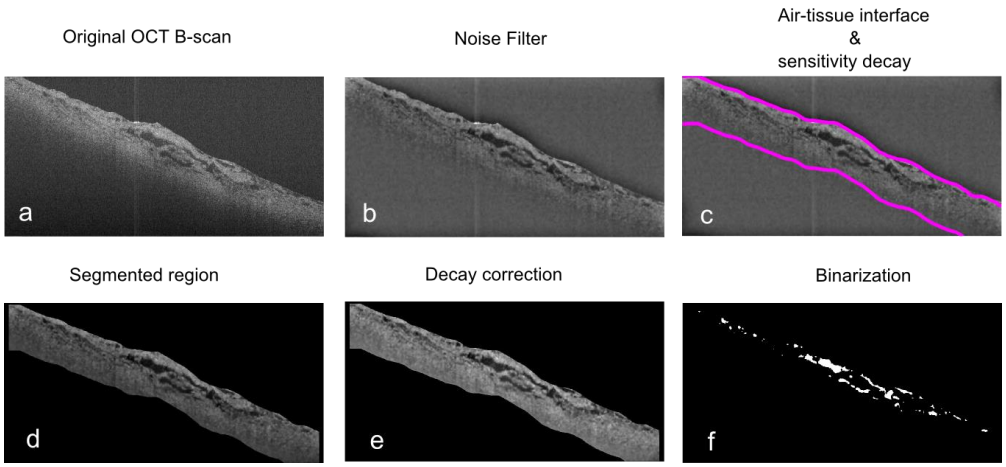

Fig. 3. OCT image pre-processing flowchart. On every B-scan (a), a noise filter is applied (b). A segmentation procedure is applied to distinguish the air-tissue interface and penetration limit sensitivity (c). After that, the segmented region (d) has its mean corrected in vertical and horizontal axes (e). Finally, a binarization algorithm is applied (f).

- Air-tissue interface (Fig. 3(c)): A hard median filter (60 by 30 pixels) is applied to the image in order to reduce noise and specular reflection artifacts. Afterwards, the OTSU thresholding technique [21] is used to delimit the mentioned surface.
- Noise filtering: two filters are applied (Fig. 3(b)). The first, an anisotropic diffusion filter aimed to reduce speckle-like noise in the image. Secondly, a Gabor wavelet filter [22, 23] is applied, aimed to enhance intensity differences for future anomalies.
- Segmentation (Fig. 3(c)): the region to be analyzed is delimited between the sample surface and the bottom of the image. The upper limit is fixed by the air-tissue interface. The lower limit is due to low sensitivity along penetration depth.
- Decay correction (Fig. 3(e)): intensity level follows an exponential decay, what affects detecting intensity anomalies. The mean value of the image is subtracted in both axes to flatten the intensity profile.
- Thresholding (Fig. 3(f)): anomalies are seen as low reflectivity areas surrounded by homogeneous high intensity regions. Anomalies can be detected establishing an appropriate threshold between intensity levels of the segmented region and the intensity level of the background. The typical procedure to establish an optimal threshold consists on discriminating the background and the foreground using the gray level histogram. For an optimal solution, these two classes must be easily differentiable [21] (Fig. 4(a)). Images obtained in this study do not present such distributions (Fig. 4(b)).

  The aim of the thresholding process is to determine and delimit the regions of anomaly. These regions present low intensity levels as the background (Fig. 4(e)), but they are placed in the region of the image corresponding to tissue (Fig. 4(d)). Firstly, the histogram of the background region is computed (Fig. 4(f)) and a preliminary threshold of 95th percentile is established. Secondly, only regions below this level in the segmented image are considered. The final threshold is computed from these regions as the mean intensity level minus 2 times its standard deviation.

#220039 - $15.00 USD Received 1 Aug 2014; revised 10 Oct 2014; accepted 14 Oct 2014; published 29 Oct 2014

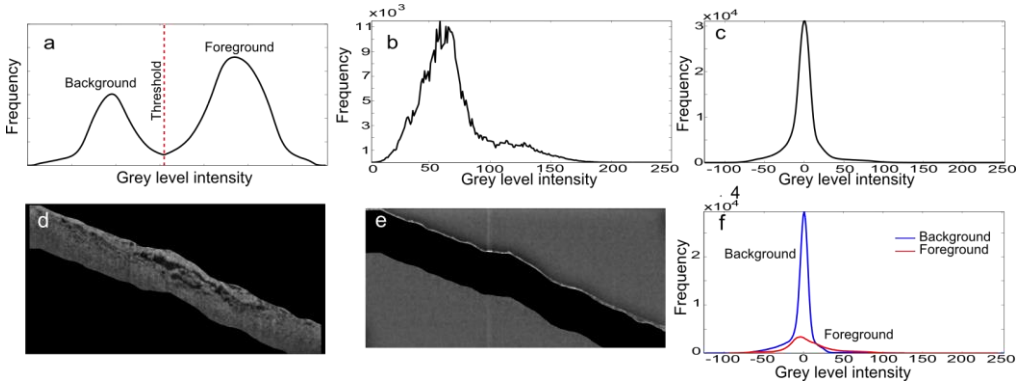

Fig. 4. Description of the thresholding procedure. Typical histogram for conventional thresholding (a) compared with histogram of OCT B-scans (b). After applying the noise filter (c), the foreground (d) and background (e) of B-scans are used to establish a threshold based on the histogram of both of them (f).

After these steps, a binary image is obtained. Anomalies are detected as regions with intensity levels lower than the threshold set in the last step. Active pixels connected among them are considered an independent anomaly region, and its area is computed as the count of adjacent pixels.

2.4 Anomalies processing

For every B-scan, the number of detected anomalies and their area is considered. The maximum area in a B-scan and the mean size of the areas are computed as criterion for further degradation assessment. In order to provide solid correlation with the histological score for degradation assessment and classification, every ROI is considered independent from the others from the same sample. As several B-scans are computed for a single ROI, this redundancy can be used to improve the characterization of the ROI and minimize the effect of inaccurate or rare B-scans occurrence. The vertical and horizontal dimensions and the orientation of detected anomalies have also been computed (Fig. 5). The major and minor dimensions of each individual anomaly has been calculated and also the orientation of the major axis in relation to the tissue surface identified on the B-scan.

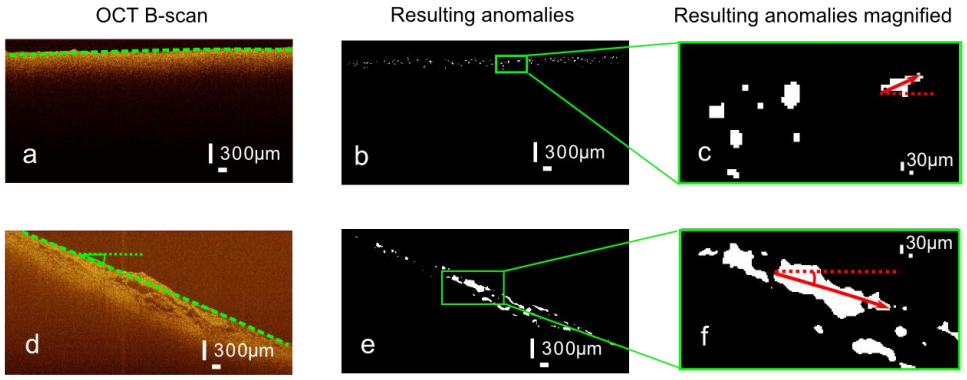

Fig. 5. Comparison of category 1 (upper) and category 2 (lower) B-scans. After the air tissue interface detection, the surface angle is computed (a, d). Anomaly areas are detected as a result of the processing algorithm (b,e). For every individual anomaly detected, the angle of the major axis is calculated in relation to the surface (c,f).

#220039 - $15.00 USD Received 1 Aug 2014; revised 10 Oct 2014; accepted 14 Oct 2014; published 29 Oct 2014

3. Results and discussion

Visual inspection of the images shows how samples showing higher scores exhibit bigger anomalies and structural disorders. Histological analysis provides higher magnification for visualization of artery cellular micro-structure, in particular anomalies associated with media layer degradation. OCT B-scans can point out these anomalies when they are bigger than the resolution of the system, in this case 12µm in depth and 25µm lateral.

3.1 Qualitative analysis

A Receiver Operating Characteristic (ROC) curve has been obtained to test pathology identification, i.e. Category 1 versus Category 2 detection. This curve is obtained varying the area of anomalies as the discrimination threshold. Every B-scan in a sample is compared with the threshold. If there are one or more areas bigger than this threshold, the B-scan is considered Category 2. The detection method uses the redundancy of several B-scans per sample to bypass misdetection due to a single B-scan misclassification. Therefore, if more than 50% B-scans in a sample are detected as Category 2, the sample itself is considered Category 2, if more than 50% B-scans are detected as Category 1, the sample is then considered Category 1. This procedure is repeated with the mean area of anomalies computed for each B-scan, providing a different ROC curve (Fig. 6).

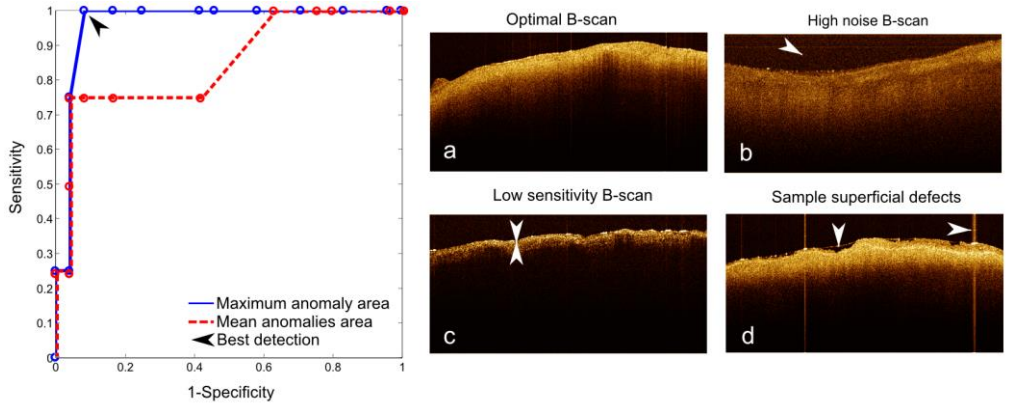

Fig. 6. Qualitative analysis results (left) considering the maximum anomaly area (blue continuous line) on every B-scan per sample, the mean anomaly area (red dashed line) of every B-scan per sample. Misclassifications on the best case (Maximum anomaly area, 120 pixels threshold) are due to high noise (b) and low sensitivity (c) on one sample and to sample superficial defects (d) when compared with the typical B-scan measured in good conditions (a).

The ROC curve resulting on Fig. 6 shows high sensitivity and high specificity for both indicators (maximum and mean anomaly areas). As the main target for this work is to detect pathological tissue regions, the best threshold will be the one that maximizes sensitivity. The results of classifying using the maximum area of anomalies present on each B-scan, provides the optimum pair sensitivity-specificity of 100%-91.6%, for an anomaly area threshold of 120 pixels (real dimension around 4965.88µm^2). According to this result, two samples are misclassified: samples 7 and 17. In the first case, the signal to noise ratio (SNR) was not enough (Fig. 6(b)), being of 20dB, in contrast with the typical SNR>50dB in the rest of the data set. Also, the dynamic range is of around 40dB (Fig. 6(b)), whilst the typical is among 60 and 80dB. Sample 17 is misclassified due to sample surface irregularities (Fig. 6(d)).

In the case of the mean anomaly area per B-scan, the best result is 75%-95% for a threshold of mean anomalies area of 13 pixels. In this case, sample 15 is not detected, due to a lower sensitivity (Fig. 6(c)) than in the rest of the data set.

#220039 - $15.00 USD Received 1 Aug 2014; revised 10 Oct 2014; accepted 14 Oct 2014; published 29 Oct 2014

3.2 Quantitative analysis

The histopathological analysis quantifies degradation according to a score from 0 to 15. As stated for the semi-quantitative grading scheme, bigger anomalies indicate a bigger degradation score in the sample. This quantification can be somehow applied to the OCT measurements, as the target is also the size of detected anomalies. Thus, a parameter able to quantify OCT anomalies in a similar way to histological analysis has been developed. For this purpose, the area of the biggest anomaly present on every B-scan has been considered. As there are several B-scans per sample, the mean value of these areas is taken as OCT quantification parameter for each sample (Fig. 7).

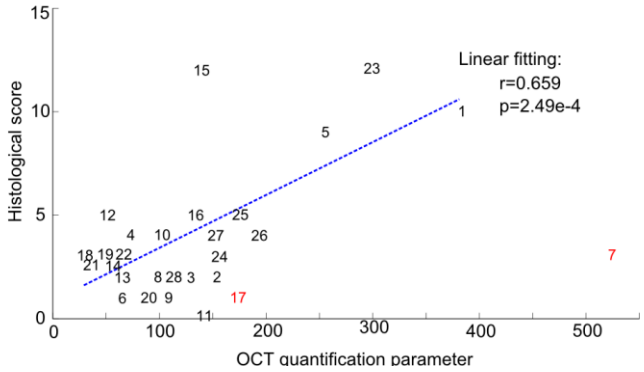

Fig. 7. Representation of the histological score versus the OCT quantification parameter. Samples 7 and 17 are discarded as they were misclassified during the qualitative analysis.

The quantification parameter has been compared with the histological score. A linear fitting has been applied to test proportionality, giving a correlation result of $r = 0.659$, with a low *p-value*. For this analysis, misclassified samples discussed in *Section 3.2* (samples 7 and 17) have been removed from the fitting.

The histological score is formed by the independent quantification of different deformations present on the analyzed tissue: fibrosis, necrosis, cystic change, SMC orientation and elastic fragmentation. According to values on Table 1, fibrosis and necrosis effect would be less relevant for the final score when compared with the rest of parameters. A linear fitting has been applied to compare the original score with a reduced semi-score formed by cystic change, SMC orientation and elastic fragmentation (Fig. 8(a)). This semi-score produces a correlation factor of $r = 0.947$ with the original score. Thus, it confirms that most of the information present in the parameters is kept in the reduced semi-score. The same quantification parameter of the maximum areas in the OCT B-scans has been tested against this reduced semi-score (Fig. 8(b)), giving a correlation of $r = 0.736$.

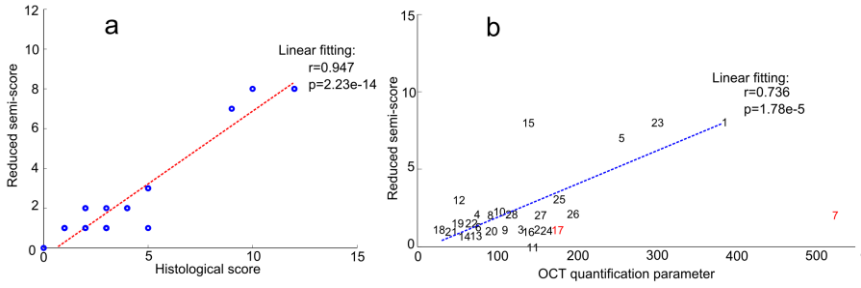

Fig. 8. Performance of the OCT degradation indicator: (a) relation between the original histological score and the reduced semi-score; (b) representation of the histological reduced semi-score versus the OCT quantification parameter. Samples 7 and 17 are discarded as they were misclassified during the qualitative analysis.

#220039 - $15.00 USD Received 1 Aug 2014; revised 10 Oct 2014; accepted 14 Oct 2014; published 29 Oct 2014

3.3 Physiological discussion

The regions of aorta considered anomalies correspond to areas with lower refraction index than the surrounding tissue. According to the pathologist, these anomalies are mainly composed of acid muccopolysacharides (n = 1.35 [24,25]), whose refractive index differs from that of collagen (n = 1.41 [26]) and the aortic media layer aggregate (n = 1.38 [18]). Therefore, the delineation of low reflectivity areas in the OCT image is equivalent to detect the presence of mucoid material within the aortic wall. The size of these areas reveals the importance of the degradation.

On the one hand, both healthy and degraded specimens present small areas of low reflection, few pixels size, without diagnostic ability. A deep study of the orientation and dimensions of detected anomalies reveals that small areas (92% of anomalies have less than 20 pixels) tend to be more spherical (Fig. 9(a)) indicating that are not related with pathological features but with small-scale heterogeneity in tissue and OCT speckle noise. As the size of the anomaly increases, one of the axes of the anomaly area gains importance and disorders tend to be oriented parallel to the sample surface, i.e. mayor axis angle close to 0° (Fig. 9(b)). As the aortic tissue morphology is organized in layers, the degradation is generally produced within a layer and its extension increases from a single lamellar unit to the adjacent ones [20]. This way, those anomalies growing in a direction parallel to the layers organization reveal pathological evidences.

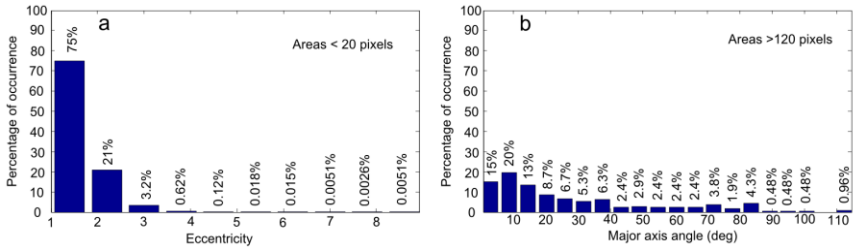

Fig. 9. Shape and orientation of OCT detected anomalies: with respect to the sample surface: (a) shape of small anomalies in terms of eccentricity; (b) distribution of orientation for anomalies greater than 120 pixels.

On the other hand, the qualitative analysis shows that areas greater than 120 pixels provide good classification performance. The mean linear dimensions of areas of 120 pixels (110 to 130) are of 22.9 pixels in the horizontal axis and 15.6 pixels in the vertical axis, again mostly horizontally oriented parallel to the tissue layers. When translated into physical dimensions, those mean dimensions of anomalies become 223.50μm lateral (horizontal) and 66.14μm axial (vertical). As shown in Table 2, the mean vertical size is on the range of the mean values for maximum degradation (score 3 out of 3) of cystic change (33.60μm) and of elastic fragmentation (84.00μm) indicating that anomalies distinguished by OCT are associated to these two effects that affect interlamellar regions of the wall. In case of fibrosis, necrosis and SMC orientation, the size for histological classification shown on Table 2 is above the ability of OCT penetration for a complete visualization of the degradation. Also, reflectivity is non homogeneous in a wide affected region, presenting areas of high reflectivity (collagen and SMC) mixed with regions of low reflectivity (mucoid).

Table 2. Dimensions of severe degradation anomalies for the histological semi-quantitative grading scheme.

	Anomaly criteria for individual score of 3/3	**Anomaly size for individual score of 3/3 ***
Fibrosis	More than 2/3 of the media layer thickness	899.79μm lateral or axial
Necrosis	More than 2/3 of the media layer thickness	899.79μm lateral or axial
Cystic change	More than 1 lamellar unit	33.60 μm axial
SMC orientation	More than 1/2 of the media layer thickness	674.84 μm lateral or axial
Elastic fragmentation	Five or more lamellar units	84.00 μm axial

***Mean values of all samples.

#220039 - $15.00 USD Received 1 Aug 2014; revised 10 Oct 2014; accepted 14 Oct 2014; published 29 Oct 2014

According to the pathological analysis, Table 1, high-degraded specimens of Category 2 present the highest scores for cystic change, elastic fragmentation and SMC orientation. These three indicators are intimately linked. The loss of muscular cells produces reduction and disorders in the number of elastic fibers and the absence of SMC and elastic fibers becomes filled with mucoid substance, what confirms the OCT results. Regarding the interpretation of fibrosis and necrosis, the degradation for a high score is severe and can be seen as great structural disorders (Fig. 10). Table 1 shows a small score for these two effects on Category 2 samples. During the quantitative analysis, it has been checked that a semi-score excluding both effects on the degradation quantification provides most of the information seen on the complete score. Fibrosis and necrosis seem to be more relevant with deformations greater than the ones seen in the samples confirming that the OCT threshold correlates with the pathological score from the cystic change and the elastic fragmentation mechanisms.

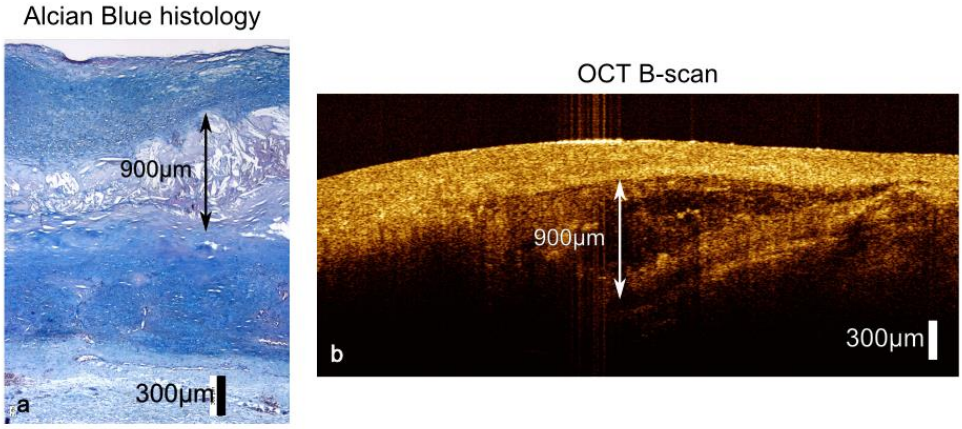

Fig. 10. Comparison of necrosis and fibrosis seen with histology (a) and OCT (b) at the same scale. Both images are from the same sample but do not represent the same exact position.

3.4 Future intraoperative application

Generally, wall degradation affects a wide aortic region. However, it slightly differs along the vessel length and circumference. The main goal for this analysis is to identify the severely degraded regions to be excised during surgical intervention and delimit the borders of the pathological tissue. Different ROIs measured on each sample are distributed along the whole sample extension. The analysis described in the previous sections has been intensively applied to these regions, computing the C-scans of 100 B-scans per ROI. After the analysis of every B-scan, a degradation map of the sample can be obtained. Degradation can be quantified on every B-scan, and this way, the degradation variation can be seen across and along each ROI (Fig. 11).

#220039 - $15.00 USD Received 1 Aug 2014; revised 10 Oct 2014; accepted 14 Oct 2014; published 29 Oct 2014

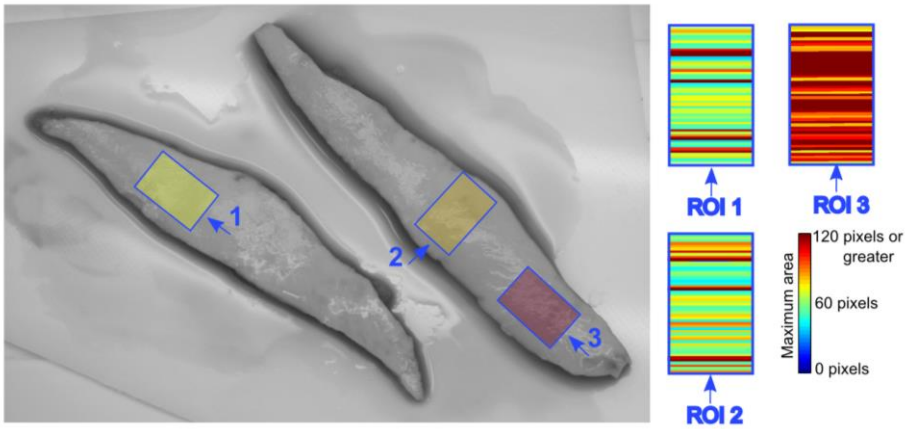

Fig. 11. Degradation on the 3 ROIs of a sample (left) quantified for every individual B-scan as the maximum anomaly size present on the B-scan. Each ROI is colored with the mean color of its degradation map (right).

It can be seen on Fig. 11 how degradation is not uniform along the whole sample. The degradation in the aorta will be a generalized phenomenon, but it is seen that it is not homogeneous on the whole vessel extension. There are also differences among individual B-scans from a single ROI. The condition of the ROI can be seen as an average of the B-scans that constitute the ROI itself. At a sample scale, regions with high degradation (ROI 3 in Fig. 11) would not be suitable for stent placing during surgical intervention, whilst low degradation (ROIs 1 and 2 in Fig. 11), would be suitable for that aim.

4. Conclusions

During the histological analysis, the extension of degradations in aorta tissue is the main parameter to quantify the pathological condition of the samples. The analysis of the OCT B-scans shows how the dimension of detected anomalies correlates with the histological quantification score. B-scans presenting anomalies bigger than a certain area identify severely degraded samples, thus, this seems a feasible classification parameter.

Degradation within a single aorta sample is generalized but not homogeneous, as it can be concluded from the analysis of different regions of the samples. In order to obtain a perfect correlation among histological information and OCT, it would be necessary to apply histopathological techniques to every region of the sample, as well as the quantification scheme. This procedure would be time consuming and difficult to implement. Even then, different cross sections within one region differ with the others in the area, and so do OCT B-scans.

It is to conclude that the general degradation of the sample can be assessed with the pathological analysis. However, OCT analysis becomes an interesting intraoperative tool for wall degradation assessment due to its straightforward application and possibility of scanning of wider vessel areas per fraction of time. These interesting findings suggest that OCT intraoperative analysis could be part of the future cardiovascular surgical armamentarium. For that aim, it is essential to ensure that the dynamic range and SNR are automatically regulated based on quality criteria, as well as the focusing distance to the sample surface.

Acknowledgments

This work has been supported by the Spanish Government through the CYCIT projects DA2TOI (FIS2010-19860) and Sensores de fibra óptica para Seguridad y Protección I (TEC2013-47264-C2-1-R).